C. R. Mecanique 346 (2018) 794–805

Contents lists available at ScienceDirect

Comptes Rendus Mecanique

www.sciencedirect.com

Computational modeling of material forming processes / Simulation numérique des procédés de mise en forme

Characterization of strain rate effects in sheet laser forming

Javier I. Castillo [a], Diego J. Celentano [a,*], Marcela A. Cruchaga [b], Claudio M. García-Herrera [b]

[a] Departamento de Ingeniería Mecánica y Metalúrgica, Centro de Investigación en Nanotecnología y Materiales Avanzados (CIEN-UC), Pontificia Universidad Católica de Chile (PUC), Av. Vicuña Mackenna 4860, Santiago, Chile
[b] Departamento de Ingeniería Mecánica, Universidad de Santiago de Chile (USACH), Av. Bernardo O'Higgins, 3363, Santiago, Chile

ARTICLE INFO

Article history:
Received 30 August 2017
Accepted 28 March 2018
Available online 18 June 2018

Keywords:
Laser forming
Plastic model
Viscoplastic model
Finite elements
Stainless steel

ABSTRACT

This work presents numerical simulations and experimental validation of sheet laser forming processes using a single-step straight path with different laser beam powers (four levels ranging from 30 W to 120 W) and scanning speeds (four levels ranging from 5 mm/s to 20 mm/s) in graphite-coated AISI 304 stainless steel 0.6-mm-thick sheets. The numerical simulations of these cases are performed via a coupled thermomechanical finite element formulation accounting for large strains, temperature-dependent material properties and convection–radiation phenomena. Firstly, a rate-independent plastic model is used. Although this model adequately predicts the final bending angle for the cases achieving relatively low maximum temperatures, i.e. cases with low laser beam powers and high scanning speeds, it fails in describing the deformation pattern for the cases with higher maximum temperatures, i.e. cases with high laser beam powers and low scanning speeds. Secondly, in order to overcome this drawback, a rate-dependent viscoplastic model including a stress-dependent viscosity law is proposed to simulate the same cases. The final bending angles provided by this model are found to be in good agreement with the experimental measurements for the whole ranges of laser beam power and scanning speed studied in this work. Therefore, the use of this viscoplastic model in the simulation of sheet laser forming allows us to conclude that the strain rate effects, which mainly play a relevant role at high temperatures, can be adequately characterized.

1. Introduction

Laser forming is a flexible and particularly suitable manufacturing technique for low-volume production and/or rapid prototyping of sheet metal components in which either forming tools or external forces are not needed [1–5]. This process allows the bending of the work piece through the development of thermomechanical strains generated by the heating of a laser beam with a given power and scanning speed. The formation of a high thermal gradient along the plate thickness is the most appropriate condition to achieve controllable bending angles. This is the so-called thermal gradient mechanism that typically occurs where the ratio between the diameter of the laser beam and the plate thickness is relatively small [6–8]. In the heating phase, once the stress exceeds the material yield strength, plastic deformations occur under a compressive

* Corresponding author.
E-mail address: dcelentano@ing.puc.cl (D.J. Celentano).

https://doi.org/10.1016/j.crme.2018.05.001
1631-0721/

stress field due to the fact that the heated region is restricted to expand by the surrounding material that is at a lower temperature. In the cooling stage, the work piece shrinks on the heated surface under tensile stresses which make the plate bend toward the laser beam. In this way, the sheet laser forming method allows flexibility, that conventional methods cannot in general achieve, combined with a good dimensional accuracy level, thus attracting interest in sectors such as the aeronautics, nanotechnology and automotive industry [9–11]. Nevertheless, a strict control of all the operating variables, e.g., laser beam diameter, power and scanning speed, is needed in order to obtain the desired final shape.

Despite all the advances in the field, the accurate description of the thermomechanical material response during laser forming is a complex task that led in recent years to the use of finite element simulations focused on different aspects of the process: effects of operating variables on the deformation field [12–26], use of non-standard forming materials [27,28], influence of edge effects [29–33], multi-scan forming [34–38], and production of complex shapes using general heating paths [39–48]. In all these works, the rate-independent plasticity theory adopted to model the material behavior provided numerical results that reasonably fit the corresponding experimental measurements. Nevertheless, it has been recognized that this approach cannot accomplish a realistic prediction of the final bending angle when the peak temperature is high compared to the melting temperature of the forming material such as those measured in cases with high-laser-beam powers and low scanning speeds [48,49] or, more precisely, in cases with high values of line energy (LE) [6–8], defined as the ratio between the laser beam power P and the scanning speed V. In this situation, the strain rate effects on the flow stress and thus deformation become quite significant, even with moderate strain rate levels [49]. Within the context of plasticity, such effects were considered via an empirical-based flow stress relationship defined in terms of the equivalent strain rate and temperature with parameters determined through uniaxial tension and/or compression tests at certain temperatures [49]. Although the computed results with this last approach were consistent with the experimental observations, a more exhaustive assessment of strain rate effects for a wide range of operating variables is still needed.

This work presents an experimental and numerical analysis of a single-pass laser-forming process applied to graphite-coated thin 0.6-mm-thick AISI 304 stainless steel sheets aimed at characterizing strain rate effects when specific combinations of laser power and scanning speeds on a linear path are used. To this end, the proposed methodology described in Section 2 consists in two stages, respectively devoted to the realization of laser bending tests and the numerical simulation of this process carried out with a coupled thermomechanical finite element formulation accounting for large strains, temperature-dependent material properties and convection–radiation phenomena. In order to assess the influence of the strain rate on the thermomechanical material response, the numerical analysis is performed via two different models: firstly, a rate-independent plastic model and, secondly, a rate-dependent viscoplastic model including a stress-dependent viscosity law specifically defined in this study. The numerical results obtained with these two models are compared and discussed in Section 3. The viscoplastic simulations are found to provide a satisfactory experimental validation of the final bending angle for the whole ranges of laser beam power and scanning speed considered in this study. Finally, the concluding remarks are presented in Section 4.

2. Methods

2.1. Experimental procedure

Set-up

In the experimental forming tests, an optical Yb-doped fiber laser with maximum nominal power of 200 W was used. The laser wavelength has a spectral range near the infrared (1060–1080 nm). This equipment has its own digital system, where the needed operating parameters of the laser beam, such as the power energy and the power delivery option (i.e. continuous, discrete or by pulses), can be determined. It is composed of the laser equipment, the optical fiber, and the collimator from where the radiation comes out. To focus the laser beam, two biconvex lenses were mounted to obtain the desired beam diameter, which in this work was adopted as 1.2 mm. In this experimental configuration, the laser system was maintained fixed, while the different plates to be formed were mounted on a CNC table, as shown in Fig. 1a (see [48] for more details).

It is important to estimate the set-up energy losses in order to calculate the real power that enters the plate. The power loss in one lens was measured with a powermeter, resulting in an average of 9.92% for a wide range of different output powers. Thus, the total power loss was considered as approximately 20% for the present device.

Material

The material used corresponds to AISI 304 stainless steel plates, with a thickness of 0.6 mm and a chemical composition shown in Table 1. The temperature-dependent thermomechanical properties of this material are plotted in Fig. 2.

Studied cases

All the experimental forming tests were performed with rectangular samples of 75 mm in length and 60 mm in width, firmly clamped in one end in order to avoid warping of the sheet; see Fig. 1b. In order to increase the amount of laser energy absorbed by the sheet, all samples were coated with a graphite layer [50]. Four levels of both laser beam power (including the energy loss) and scanning speed were considered in the tests, resulting in a total of 16 different cases obtained by a combination of power and scanning speed values labeled as: $P_1 = 30$ W, $P_2 = 60$ W, $P_3 = 90$ W, $P_4 = 120$ W,

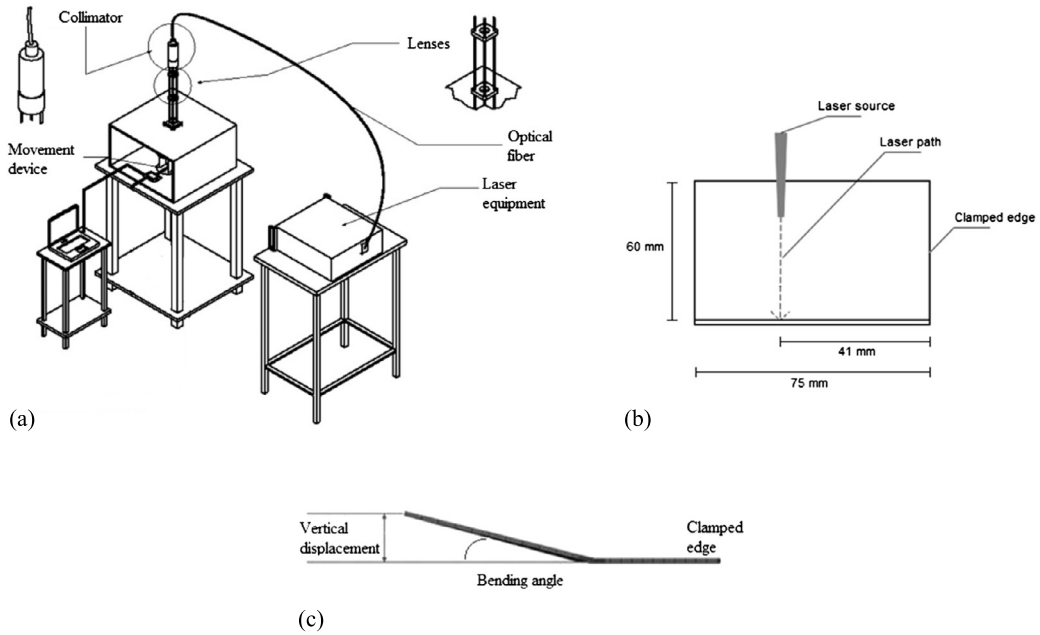

Fig. 1. (a) Components of the experimental set-up, (b) sample dimensions and (c) bending angle definition.

Table 1
Chemical composition of AISI 304 stainless steel [20].

C min	Mn	Si	P	S	Cr	Ni	Fe
0.08	2.00	1.00	0.05	0.03	18–20	8–11	Bal.

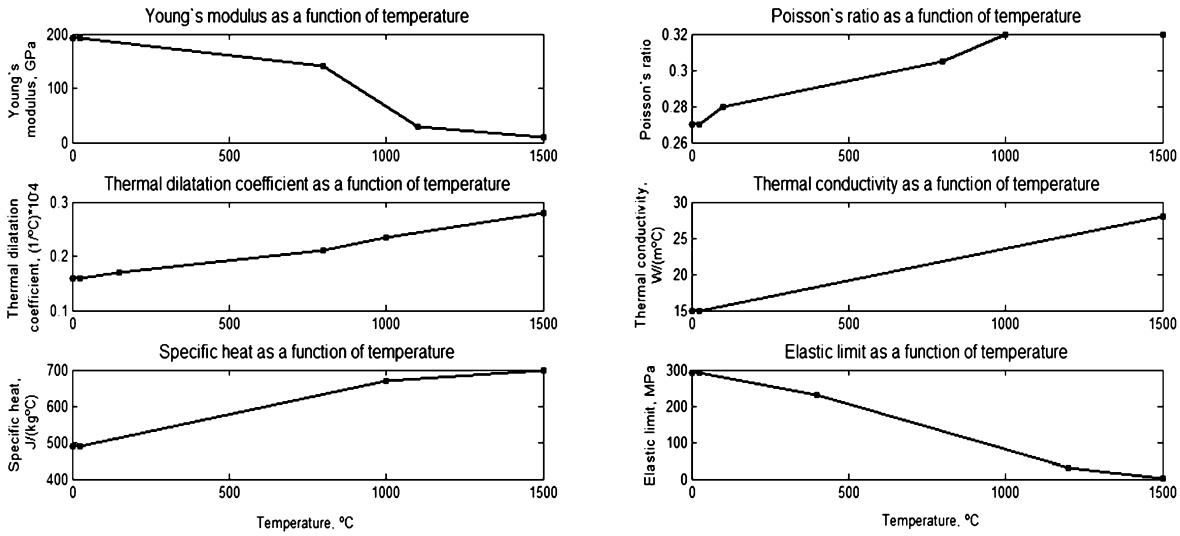

Fig. 2. Temperature-dependent thermal and mechanical properties of the AISI 304 stainless steel [26].

and $V_1 = 5$ mm/s, $V_2 = 10$ mm/s, $V_3 = 15$ mm/s, $V_4 = 20$ mm/s. To achieve statistically reliable data, 7 experiments were made for each case.

The resulting bending angle in all cases was measured, via a photo imaging software [20,48], as the average between those at the beginning and end of the laser beam path; see Fig. 1c. Due to the negligible bending angle exhibited by cases P1V3, P1V4 and P2V4 (combinations of low power with high scanning speed that result in a nearly elastic reversible response), they were excluded from the analysis. Therefore, the studied cases correspond to 13. Moreover, it should be noted that the adopted values for the operating parameters caused in all cases both the development of temperature gradients along the plate thickness and practically negligible edge effects during the process.

Table 2
Thermomechanical formulation.

Governing equations (written in a Lagrangian description)	
Continuity equation	$\rho J = \rho_0$
Equation of motion	$\nabla \cdot \boldsymbol{\sigma} = \mathbf{0}$
Energy balance equation	$-\rho c \dot{T} - \nabla \cdot \mathbf{q} = 0$

all of them valid in the domain $\Omega \times \gamma$, where Ω is the spatial configuration of a body and γ is the time interval of interest, where:

- J is the Determinant of the deformation gradient tensor $\mathbf{F}$ (where $\mathbf{F^{-1}} = \mathbf{I} - \nabla \boldsymbol{u}$, $\mathbf{I}$ being the unity tensor and $\boldsymbol{u}$ is the displacement field);
- ρ is density;
- ∇ is the spatial gradient operator;
- $\boldsymbol{\sigma}$ is the Cauchy stress tensor (symmetric for the nonpolar case adopted in this work);
- c is the specific heat capacity, taken from Fig. 2;
- T is the temperature of the body;
- $\mathbf{q}$ is the heat flux vector;
- Subscript 0 denotes values in the initial configuration Ω_0.

The effects of body forces, acceleration, external heat source and heat due to mechanical work are assumed to be negligible.

Thermal boundary conditions

The normal heat flux boundary condition of the energy balance (considered valid in $\Gamma_f x \gamma$, where Γ_f is the thermal boundary of the spatial configuration Ω) is written as:

$$\mathbf{q} \cdot \mathbf{n} = q_c + q_l$$

where q_c is the convection–radiation normal heat flux, q_l is the normal heat flux provided by the laser beam and $\mathbf{n}$ is the outward unit normal vector to Γ_f. The following laws are adopted:

$$q_c = -h_{cr}(T - T_{env})$$
$$q_l = -a f_l(P_l, d_l)$$

where:

- h_{cr} is the convection–radiation heat transfer coefficient;
- T_{env} is the environmental temperature;
- a is the absorption coefficient, taken as 0.64 [50];
- f_l is the laser heat flux distribution function, with P_l and d_l the power and the diameter of the laser beam, respectively. In this work, a Gaussian distribution is adopted: $f_l = \frac{8P_l}{\pi d_l^2} e^{-\frac{8r^2}{d_l^2}}$, where r is the radial distance to the center of the laser beam.

A parallel convection–radiation mechanism is typically assumed, i.e. $h_{cr} = h_c + h_r$ with h_c and h_r the convection and radiation coefficients, respectively. In this work, a constant value of 9.8 W/m^2·K is adopted for h_c [20] while the radiation is described in this context as $h_r = \varepsilon \sigma_B (T + T_{env})(T^2 + T_{env}^2)$, where ε is the emissivity coefficient, taken as 0.25 [20], and σ_B is the Boltzmann constant.

Constitutive relations	
Isotropic Fourier's law	$\mathbf{q} = -k \nabla \mathbf{T}$
Stress–strain relation	$\boldsymbol{\sigma} = \mathbf{C} : (\mathbf{e} - \mathbf{e}_P - \mathbf{e}_{th})$
Thermal Almansi strain tensor	$\mathbf{e}_{th} = \frac{1}{2}\left[1 - (1 - a_{th})^{2/3}\right]\mathbf{I}$

where:

- k is the conductivity coefficient, taken from Fig. 2;
- $\mathbf{C}$ is the isotropic elastic constitutive tensor, where Young's modulus and Poisson's ratio are taken from Fig. 2;
- $\mathbf{e}$ is the Almansi strain tensor ($\mathbf{e} = 1/2\ (\mathbf{I} - \mathbf{F^{-T}F^{-1}})$);
- $\mathbf{e}_p$ is the plastic Almansi strain tensor;
- a_{th} is the thermal dilatation function ($a_{th} = \alpha_{th}\,(T - T_o)$, with α_{th} the thermal dilatation coefficient, taken from Fig. 2).

It should be noted that the adopted stress–strain relation is written in therms of the Cauchy stress, instead of the Kirchhoff stress, since both measures are practically identical in this formulation because the determinant of the deformation gradient is nearly one due to the consideration of small thermoelastic strains and plastic strain rates governed by the von Mises (isochoric) flow rule.

Von Mises yield function	$F = \sqrt{3J_2} - C_{Y_0} - C$

where J_2 is the second invariant of the deviatoric part of $\boldsymbol{\sigma}$ ($\sigma_{eq} = \sqrt{3J_2}$ is the so-called equivalent or von Mises stress), C is the plastic isotropic hardening function and C_{Y_0} is the yield strength, taken from Fig. 2, defining the initial material elastic bound.

Hardening function	$C = A^P \overline{e_p}^{n^p}$

where:

- A^P is the hardening coefficient, defined through a linear relationship (450 MPa at 20 °C and 0.1 MPa at 1500 °C);
- n^p is the hardening exponent, taken as 0.2;
- $\overline{e_P}$ is the equivalent plastic deformation.

(*continued on next page*)

Table 2 (*continued*)

Plastic model	
Flow rule	$L_v\left(\mathbf{e}_{\mathrm{p}}\right)=\dot{\lambda}\frac{\partial F}{\partial \boldsymbol{\sigma}} \qquad \dot{\bar{e}_{\mathrm{p}}}=-\dot{\lambda}\frac{\partial F}{\partial C}$
where:	
L_v	is the Lie (frame-indifferent) derivative;
$\dot{\lambda}$	is the plastic consistency parameter (derived from the condition $\dot{F}=0$).
Viscoplastic model	
Flow rule	$L_v\left(\mathbf{e}_{\mathrm{p}}\right)=\lambda\frac{\partial F}{\partial \boldsymbol{\sigma}} \qquad \dot{\bar{e}_p}=-\lambda\frac{\partial F}{\partial C}$ $\lambda=\left\langle\frac{F}{K}\right\rangle^m$ $K=b\,\sigma_{\mathrm{eq}}$
where:	
λ	is the viscoplastic parameter;
$\langle\,\rangle$	are the Macauley brackets;
K	is the viscosity of the material;
m	is the strain rate sensitivity exponent, taken as 7.0 [54];
b	is the viscous coefficient, taken as 1.0 $\mathrm{s}^{1/m}$.

2.2. Thermomechanical formulation

The thermomechanical formulation used in the simulations carried out in this research is based on that reported in [20] where a plastic, i.e. rate-independent, material response was firstly assumed. Such approach is extended in the present work through a viscoplastic model to account for rate-dependent effects that are apparent in the studied forming tests where combinations of high power with low scanning speed are considered leading, as already mentioned, to relatively high peak temperatures. The adopted viscoplastic model is based on investigations devoted to find rate-dependent models able to explain the variables behavior in processes where metals (mainly steel) reach high temperatures in a short period of time [51–54].

The full thermomechanical formulation is summarized in Table 2. The plastic and viscoplastic constitutive models employed and assessed in the simulations presented in Section 3 are also included where, in particular, the proposed stress-dependent viscosity law is found to properly predict, unlike the plastic law, the final bending angle for the whole ranges of laser beam power and scanning speed studied in this work. Although alternative definitions of the viscoplastic parameter λ have been proposed in the literature [49,51–53], they were precluded from the present study due to their complex characterization since they usually involve more material parameters than those appearing in the expression included in Table 2.

2.3. Numerical simulation

The solution to the thermomechanical formulation presented above was tackled in the context of the finite element method via an in-house code extensively validated in many engineering applications, including traditional and laser forming processes [20,54–57]. The numerical solution to the resulting coupled discretized equations is achieved by using a staggered scheme in combination with an improved isothermal split, which preserves the coupling degree and provides unconditional stability. In this framework, the well-known total Lagrangian approach under isothermal conditions is considered for the mechanical problem, while the solution to the thermal problem is done with the spatial configuration assuming a fixed elastic configuration. Furthermore, the line search technique is also employed with the Newton–Raphson iterative procedure to accelerate the numerical convergence. Moreover, the integration of the temperature rate is carried out with the generalized midpoint rule algorithm choosing the parameter that makes this procedure unconditionally stable. This scheme has also been used to integrate the viscoplastic rate equation via a return-mapping procedure. Finally, in order to overcome the volumetric locking effect on the numerical solution when incompressible plastic flows are considered, like that resulting from the von Mises flow rule described above, an enhanced strain–displacement matrix classified within the B-bar methods is used in the present analysis. Details of the numerical approach can be found elsewhere [55,56].

To simulate the studied laser forming cases described above, the plate was spatially discretized with the mesh depicted in Fig. 3a. The elements used are hexahedral, with one transition such that a fine discretization is considered on the laser path to properly capture the expected high gradients of the thermomechanical variables; see Fig. 3b. The problem has been solved with a time step of 0.01 s. The initial and environment temperatures in all cases corresponded to 25 °C.

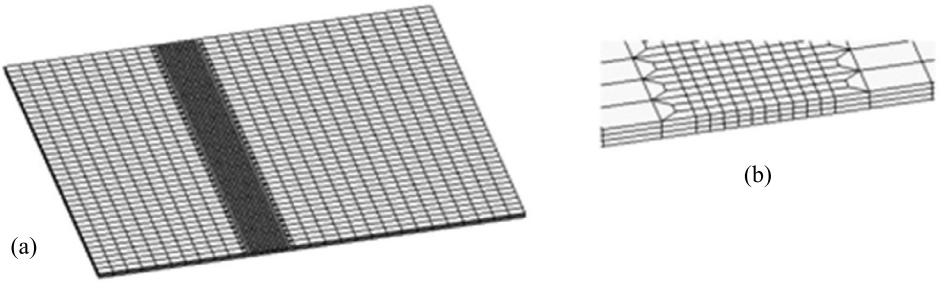

Fig. 3. Finite element mesh of the plate: (a) whole domain and (b) detail on the refined zone along the laser beam path.

Table 3
Experimental and numerical bending angles.

Case	Line energy (LE) P/V (J/mm)	Experimental angle (°)	Numerical angle (°)		Relative numerical error with respect to the experiment (%)	
			Plastic model	Viscoplastic model	Plastic model	Viscoplastic model
P1V1	6	0.97 ± 0.10	0.93	0.90	4.1	7.2
P2V1	12	2.96 ± 0.36	1.89	2.81	36.1	5.1
P3V1	18	4.16 ± 0.49	2.09	4.23	49.8	1.7
P4V1	24	4.28 ± 0.50	1.97	4.62	54.0	7.9
P1V2	3	0.47 ± 0.14	0.55	0.50	17.0	6.4
P2V2	6	1.50 ± 0.20	1.36	1.38	9.3	8.0
P3V2	9	2.68 ± 0.16	1.83	2.68	31.7	0.0
P4V2	12	3.23 ± 0.48	1.88	2.98	41.8	7.7
P2V3	4	1.05 ± 0.11	1.01	0.97	3.8	7.6
P3V3	6	1.73 ± 0.31	1.73	1.86	0.0	7.5
P4V3	8	2.48 ± 0.29	1.94	2.45	21.8	1.2
P3V4	4.5	1.67 ± 0.08	1.65	1.68	1.2	0.60
P4V4	6	1.96 ± 0.19	2.07	2.10	5.6	7.1

Combinations between laser beam power (P) and scanning speed (V) are labeled as P1 (30 W), P2 (60 W), P3 (90 W) and P4 (120 W), and V1 (5 mm/s), V2 (10 mm/s), V3 (15 mm/s) and V4 (20 mm/s).

3. Results and discussion

3.1. Bending angle

Table 3 summarizes the experimental average values of bending angles, with their corresponding standard deviation, for the cases studied. The line energy (LE) values for each case are also detailed. As expected, higher bending angles are generated for increasing levels of laser beam power and decreasing values of scanning speed. These measurements are compared with the respective numerical results using both the plastic and viscoplastic models (see Table 2). It is seen that the results for both models are very similar when LE $\leq$ 6 J/mm (i.e. cases P1V1, P1V2, P2V2, P2V3, P3V3, P3V4, P4V4), whereas they begin to differ when LE $\geq$ 8 J/mm (i.e. cases P2V1, P3V1, P4V1, P3V2, P4V2, P4V3). In these last configurations, the viscoplastic model is clearly more accurate than the plastic one. Furthermore, unlike the plastic model, the viscoplastic model predicts bending angles that, in accordance with the experiments, increase for both higher laser beam powers at a given scanning speed value and lower laser beam scanning speeds at a given power. In all cases, the bending angles computed with the viscoplastic model fall within the experimental uncertainty range (note that this is not the case for the plastic model predictions exhibiting an error greater than 20%).

3.2. Computed thermomechanical variables

This section presents and compares the computed evolution during a specific time interval of the most relevant thermomechanical variables of the process at a representative node located in the heated surface at the middle of the laser scanning path. Figs. 4 to 7 respectively show the results corresponding to the cases with the four scanning speed levels considered in this study.

The temperature peaks follow, as expected, the same trend as that of the bending angles, i.e. higher temperature peaks are predicted for increasing levels of laser beam power and decreasing values of scanning speed. For each scanning speed, the temperature rate peaks also increase with higher laser beam powers. However, for a given laser beam power, the effect of the scanning speed on the temperature and temperature rate peaks has the opposite behavior, i.e. higher temperature rates develop for increasing scanning speeds, with a nearly linear proportional ratio between them.

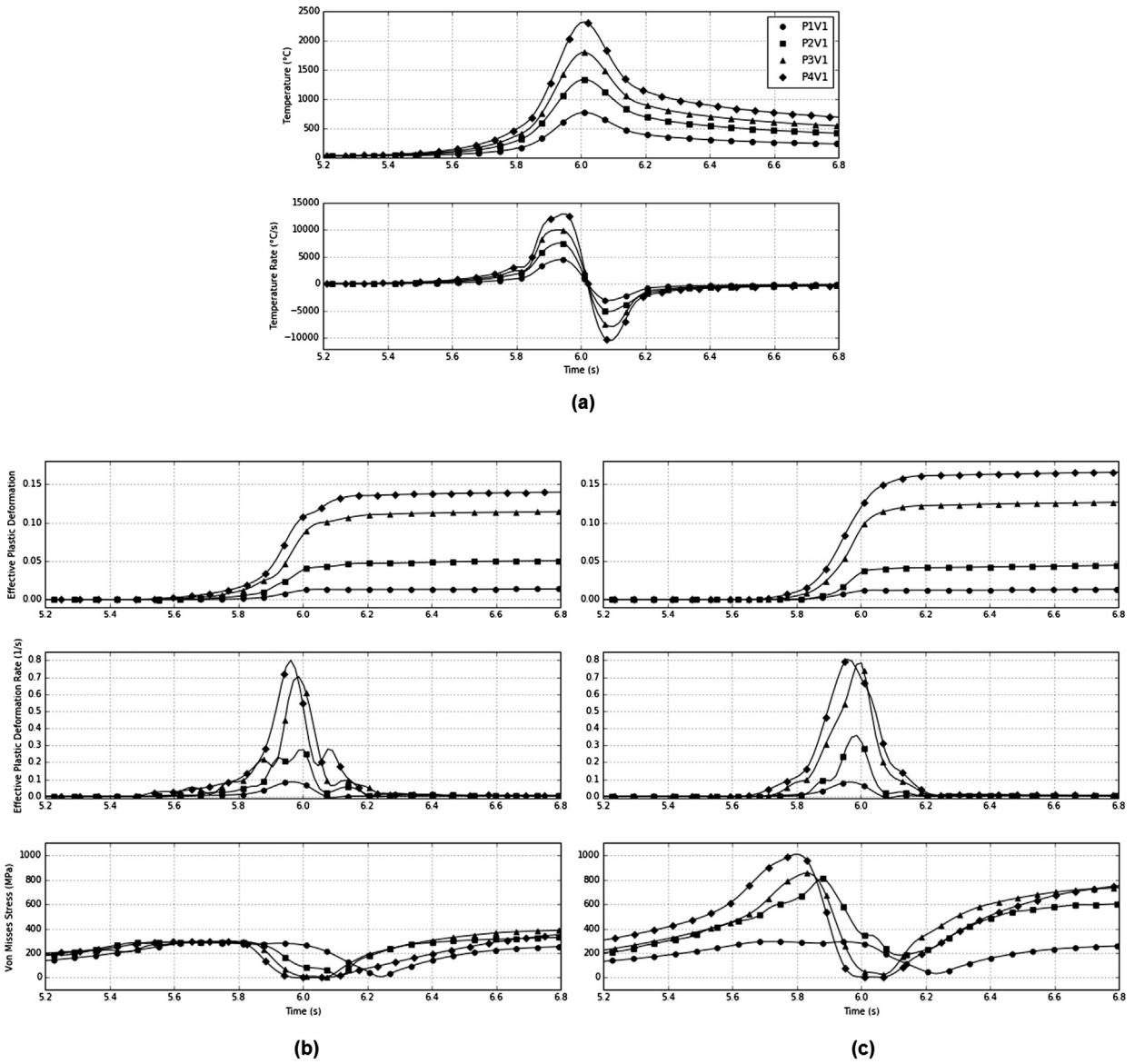

Fig. 4. Computed evolution of variables at a heated point for different laser beam power values and a scanning speed $V_1 = 5$ mm/s: (a) temperature and temperature rate; effective plastic deformation, effective plastic deformation rate, and von Mises stress for (b) plastic and (c) viscoplastic models.

As mentioned above, pronounced temperature gradients occur along the plate thickness, thus confirming that the deformation is mainly caused by the thermal gradient mechanism. The maximum difference between the temperatures at the top and bottom surfaces of the plate depends for all cases exclusively on the laser beam power, i.e. it is nearly independent of the scanning speed: 370 °C, 650 °C, 890 °C and 1140 °C for P_1, P_2, P_3, and P_4, respectively.

The equilibrium melting temperature range of the AISI 304 stainless steel is [1400–1450 °C]. The cases together with the time intervals in which the solidus temperature is exceeded are: P3V1 (0.12 s), P4V1 (0.20 s), P3V2 (0.02 s), P4V2 (0.06 s), P4V3 (0.03 s) and P4V4 (0.02 s). A qualitative metallographic analysis of these cases was carried out in order to assess possible microstructural changes. Fig. 8 shows micrographs corresponding to the heated zone of the sample for the cases with higher LE values (i.e. P2V1, P3V1, P4V1 and P4V2), where it is seen that melting (and subsequent solidification) is only observed in the case P4V1, at a depth of approximately half of the thickness (note that finer grain sizes and dendrites at the bottom of the image, which corresponds to the place where the solidification started once the effect of the laser ceased, can clearly be appreciated). Although this case was additionally simulated including latent heat release/absorption and phase-change deformation (results not shown), these phenomena were found to have practically no effect on the final bending angle due to the fast heating and cooling temperature rates respectively present during melting and solidification.

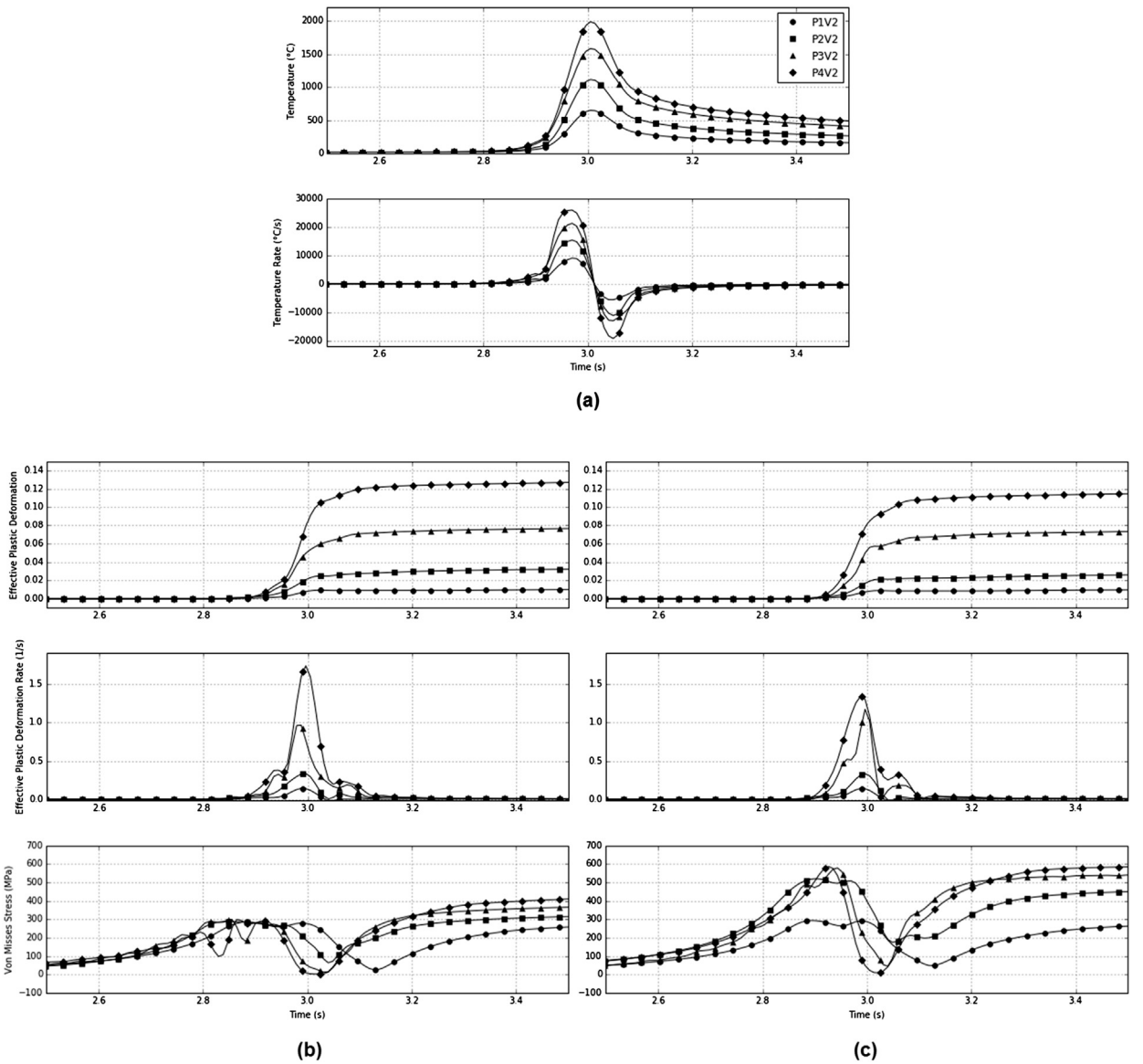

Fig. 5. Computed evolution of variables at a heated point for different laser beam power values and a scanning speed $V_2 = 10$ mm/s: (a) temperature and temperature rate; effective plastic deformation, effective plastic deformation rate, and von Mises stress for (b) plastic and (c) viscoplastic models.

Moreover, in the other cases, melting was presumably precluded owing to the very short time intervals with temperatures above the solidus temperature.

The effective plastic deformation also reproduces the same pattern of temperature peaks, i.e. higher effective plastic deformation levels are achieved for increasing values of laser beam power values and decreasing values of scanning speed. Nevertheless, it should be noted that a direct correlation between the bending angle and the effective plastic deformation can only be established for the viscoplastic predictions of these two variables since, although the effective plastic deformation levels are similar for both the plastic and viscoplastic models in all configurations, inaccurate bending angles computed with the plastic model are obtained, as already commented, for the cases with high line energy values (i.e. LE $\geq$ 8 J/mm). In addition, the trend of the effective plastic deformation rate is similar to that of the temperature rate. For the cases with high LE values, it is seen that strain rate levels within the range [0.35–1.60 s^{-1}] take place, thus ratifying the significant effect, as already noted in [49], that even moderate strain rates have on the deformation when high temperatures are reached.

For the cases with low LE values, the von Mises stress evolutions respectively computed using the plastic and viscoplastic models are very similar for each case. However, for the cases with high LE values, there is a noticeable difference between the plastic and viscoplastic results in the von Mises stress levels during the laser beam pass. In such time interval, the resulting high temperatures make the thermal softening effect become relevant, i.e. both the plastic isotropic hardening

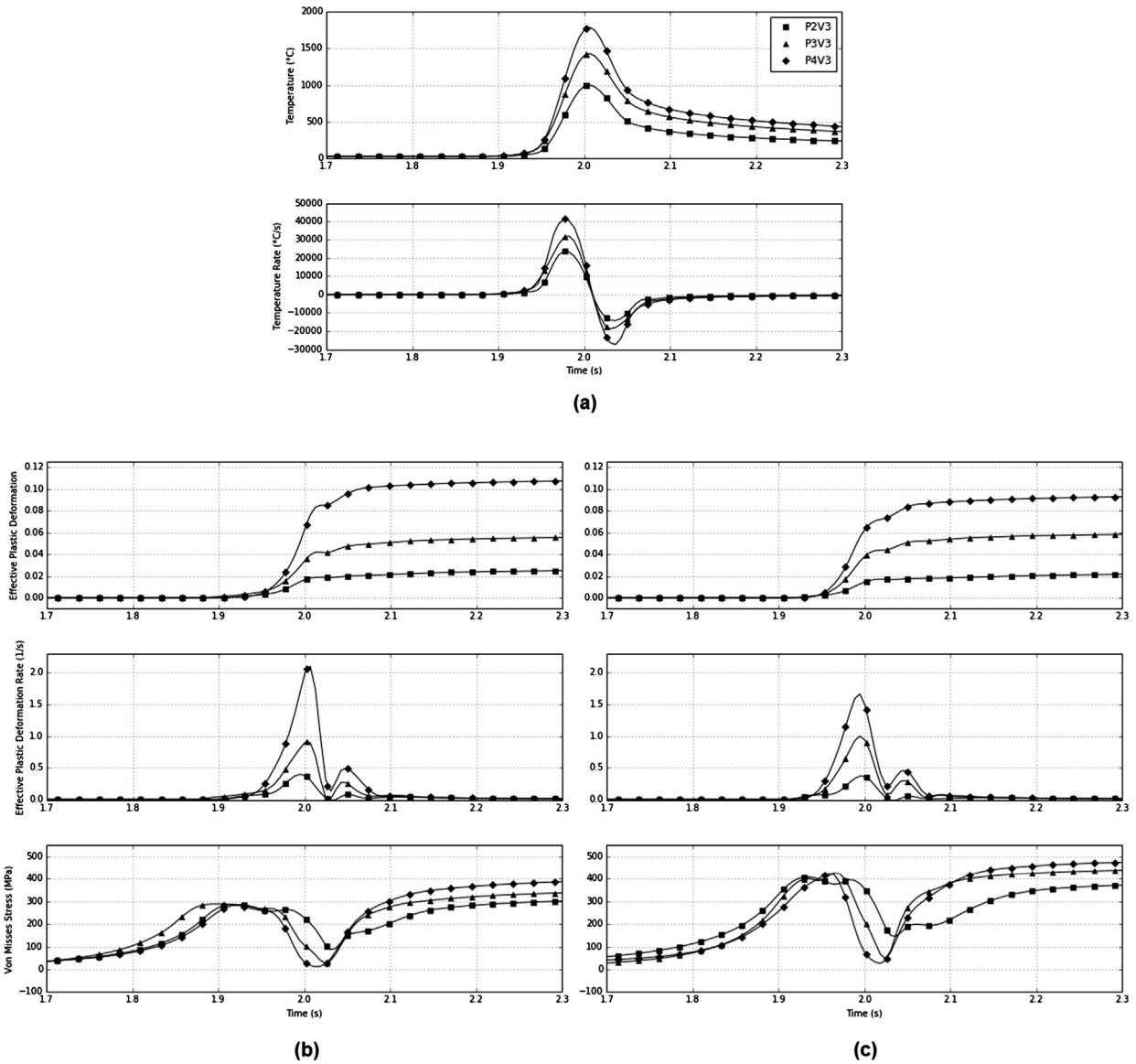

Fig. 6. Computed evolution of variables at a heated point for different laser beam power values and a scanning speed $V_3 = 15$ mm/s: (a) temperature and temperature rate; effective plastic deformation, effective plastic deformation rate, and von Mises stress for (b) plastic and (c) viscoplastic models.

function C and yield strength C_{Y_0} present their minimum values. While very low stress values are predicted by the plastic model (which is consistent with the condition $F = \sigma_{\text{eq}} - C_{Y_0} - C = 0$), the viscoplastic model furnishes, during both the heating and cooling stages, higher stress levels that, in general, increase with the decrease in the scanning speed. In particular, the high von Mises stress values that develop in the heating stage cause most of the effective plastic deformation and, hence, significantly contribute to the final bending angle. The over-stress generated at high temperatures is properly described by the proposed stress-dependent viscosity law. It should be noted that numerical tests not reported here corroborated that a purely temperature-dependent viscosity law was not able to capture this phenomenon. Furthermore, additional numerical tests also showed that a temperature-dependent function for the strain rate sensitivity exponent m, like those used in [49,51–53], in which m typically decreases with temperature, had no relevant influence on the final bending angle. Therefore, for simplicity, a constant value for this parameter was considered in the viscoplastic flow rule considered in the present simulations (see Table 2).

4. Conclusions

Finite element simulations and experimental validation of sheet laser forming processes using a single-step straight path with different laser beam powers and scanning speeds in graphite-coated AISI 304 stainless steel 0.6-mm-thick sheets have

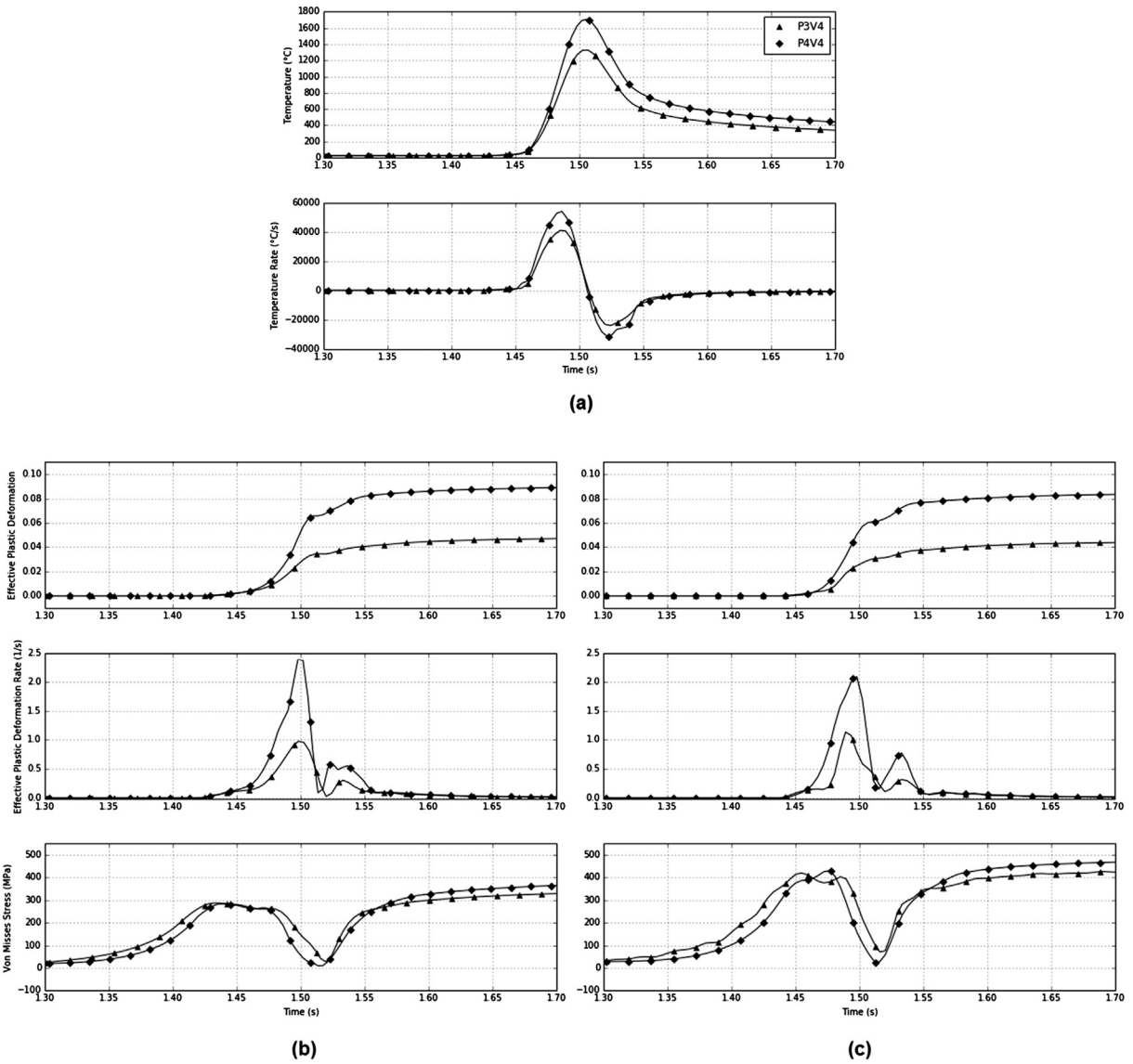

Fig. 7. Computed evolution of variables at a heated point for different laser beam power values and a scanning speed $V_4 = 20$ mm/s: (a) temperature and temperature rate; effective plastic deformation, effective plastic deformation rate, and von Mises stress for (b) plastic and (c) viscoplastic models.

been presented. The numerical analysis of these cases was separately carried out via two constitutive models respectively defined in the contexts of rate-independent plasticity and rate-dependent viscoplasticity. The plastic model was found to adequately predict the final bending angles only for those cases in which the maximum temperatures were relatively low. On the contrary, the final bending angles computed with the viscoplastic model were in good agreement with the experimental measurements for the whole ranges of laser beam power and scanning speed studied in this work. In particular, the proposed stress-dependent viscosity law was demonstrated to properly describe the over-stress that develops at high temperatures, which, in turn, is responsible for the large bending angles achieved in the cases with high line energy values. Therefore, from these results, it is possible to conclude that a sound characterization of the influence of strain rate on the thermomechanical material's response in sheet laser forming has been accomplished.

Future research will be devoted to further experimental validation of the viscoplastic model used in this work in its application to laser forming processes of different materials using single and multiple complex beam paths.

Acknowledgements

The supports provided by the National Council for Scientific and Technological Research CONICYT (FONDECYT Project No. 1180591) and the Scientific Research Project Management Department of Research, Development and Innovation

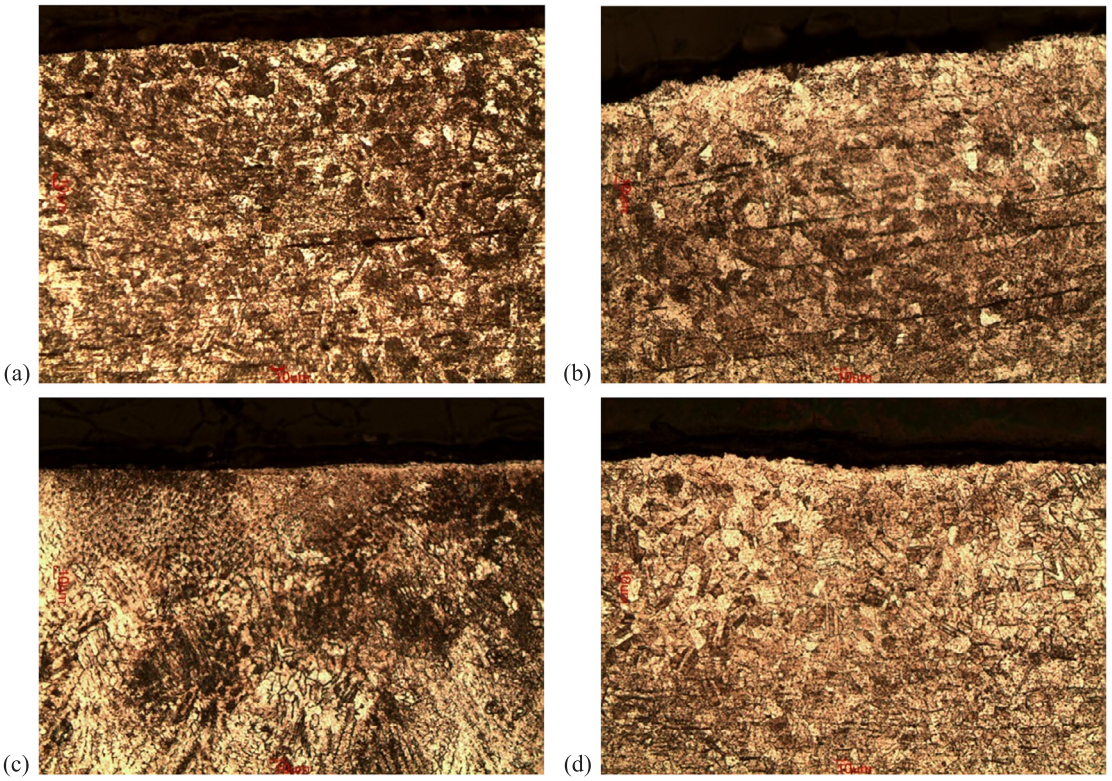

Fig. 8. Micrographs corresponding to the heated zone of the sample (200 × and 2% nital etching) for cases: (a) P2V1, (b) P3V1, (c) P4V1 and (d) P4V2.

(DICYT-VRID) at Universidad de Santiago de Chile (Proyecto Fortalecimiento Usach USA1799_GC131612) are gratefully acknowledged.

References

[1] F. Vollerstsen, Applications of lasers for flexible shaping processes, in: Proceedings of the 12th International Congress, LASER'95, Meisenbach, 1995, pp. 151–162.
[2] J. Magee, K.G. Watkins, W.M. Steen, Advances in laser forming, J. Laser Appl. 10 (1998) 235–246.
[3] S.P. Edwardson, Laser Forming Dish Shapes – A 3D Case Study, M.Sc. (Eng.) Thesis, The University of Liverpool, UK, 1999.
[4] N. Dahotre, S. Harimkar, Laser Fabrication and Machining of Materials, Springer, New York, USA, 2008.
[5] V. Paunoiu, E.A. Squeo, F. Quadrini, C. Gheorghies, D. Nicoara, Laser bending of stainless steel sheet metals, Int. J. Mater. Forum Supply 1 (2008) 1371–1374.
[6] M. Geiger, F. Vollertsen, The mechanism of laser forming, CIRP Ann. 42 (1993) 301–304.
[7] Y. Shi, Z. Yao, H. Shen, J. Hu, Research on the mechanisms of laser forming for the metal plate, Int. J. Mach. Tools Manuf. 46 (2006) 1689–1697.
[8] H. Shen, F. Vollertsen, Modelling of laser forming – a review, Comput. Mater. Sci. 46 (2009) 834–840.
[9] J. Magee, K.G. Watkins, W.M. Steen, N.J. Calder, J. Sidhu, J. Kirby, Laser forming of aerospace alloys, in: Proceedings of ICALEO'97, Section E, 1997, pp. 156–165.
[10] J. Magee, K.G. Watkins, W.M. Steen, R.L. Cooke, J. Sidhu, Development of an integrated laser forming demonstrator system for the aerospace industry, in: Proceedings of ICALEO'98, Section E, 1998, pp. 141–150.
[11] H. Frackiewicz, High-technology metal forming, in: Industrial Laser Review, 1996, pp. 15–17.
[12] Z. Hu, M. Labudovic, H. Wang, R. Kovacevic, Computer simulation and experimental investigation of sheet metal bending using laser beam scanning, Int. J. Mach. Tools Manuf. 41 (2001) 589–607.
[13] W. Shichun, J. Zhong, FEM simulation of the deformation field during the laser forming of sheet metal, J. Mater. Process. Technol. 121 (2002) 269–272.
[14] G. Yanjin, S. Sheng, Z. Guoqun, L. Yiguo, Finite element modeling of laser bending of pre-loaded sheet metals, J. Mater. Process. Technol. 142 (2003) 400–407.
[15] L. Zhang, E.W. Reutzel, P. Michaleris, Finite element modeling discretization requirements for the laser forming process, Int. J. Mech. Sci. 46 (2004) 623–637.
[16] P. Cheng, Y. Fan, J. Zhang, Y.L. Yao, D.P. Mika, W. Zhang, M. Graham, J. Marte, M. Jones, Laser forming of varying thickness plate – Part I: process analysis, J. Manuf. Sci. Eng. 128 (2006) 634–641.
[17] P. Cheng, Y. Fan, J. Zhang, Y.L. Yao, D.P. Mika, W. Zhang, M. Graham, J. Marte, M. Jones, Laser forming of varying thickness plate – Part II: process synthesis, J. Manuf. Sci. Eng. 128 (2006) 642–650.
[18] H. Shen, Z.Q. Yao, Analysis of varying velocity scanning schemes on bending angle in laser forming, in: International Workshop on Thermal Forming and Welding Distortion, 2008, pp. 215–227.
[19] J.M.S. Che, M.A. Sheikh, L. Li, A numerical study of the temperature gradient mechanism in laser forming using different laser beam geometries, Lasers Eng. 22 (2011) 413–428.
[20] V. Stevens, D. Celentano, J. Ramos-Grez, M. Walczak, Experimental and numerical analysis of low output power laser bending of thin steel sheets, J. Manuf. Sci. Eng. 134 (2012) 031010.

[21] T.M. Smith, P. Michaleris, E.W. Reutzel, B. Hall, Finite element model of pulsed laser forming, in: Proceedings of LPM2012 – the 13th International Symposium on Laser Precision Microfabrication, 2012.
[22] M. Hoseinpour Gollo, H. Moslemi Naeini, G.H. Payganeh, S. Ding, S.M. Mahdavian, Experimental analyses of bending angle by a pulsed Nd: YAG laser in sheet metal forming process, Sci. Res. Essays 7 (2012) 279–287.
[23] M. Safari, M. Farzin, A. Ghaei, Introduction into the effects of process parameters on bending angle in the laser bending of tailor machined blank based on a statistical analysis, J. Laser Appl. 25 (2013) 1–10.
[24] K. Maji, R. Shukla, A.K. Nath, D.K. Pratihar, Finite element analysis and experimental investigations on laser bending of AISI304 stainless steel sheet, Proc. Eng. 64 (2013) 528–535.
[25] M. Safari, Numerical investigation of the effect of process and sheet parameters on bending angle in the laser bending process, World J. Mech. 4 (2014) 97–101.
[26] S. Gautam, S. Singh, U. Dixit, Laser forming of mild steel sheets using different surface coatings, lasers based manufacturing, in: Topics in Mining, Metallurgy and Materials Engineering, 2015.
[27] F.R. Liu, K.C. Chan, C.Y. Tang, Numerical simulation of laser forming of aluminum matrix composites with different volume fractions of reinforcement, Mater. Sci. Eng. A, Struct. Mater.: Prop. Microstruct. Process. 458 (2007) 48–57.
[28] D. Wu, K. Zhang, G. Ma, Y. Guo, D. Guo, Laser bending of brittle materials, Opt. Lasers Eng. 48 (2010) 405–410.
[29] J. Magee, K.G. Watkins, W.M. Steen, N. Calder, J. Sidhu, J. Kirby, Edge effects in laser forming, in: Laser Assisted Net Shape Engineering 2, Proc. LANE 2 (1997) 399–408.
[30] J. Bao, Y.L. Yao, Analysis and prediction of edge effects in laser bending, J. Manuf. Sci. Eng. 123 (2001) 53–61.
[31] Y. Shi, H. Shen, Z.Q. Yao, J. Liu, Edge effects of metal plate in laser forming, Trans. Nonferr. Met. Soc. China 15 (2005) 260–263.
[32] G.C. Jha, A.K. Nath, S.K. Roy, Study of edge effect and multi-curvature in laser bending of AISI 304 stainless steel, J. Mater. Process. Technol. 197 (2008) 434–438.
[33] H. Shen, J. Hu, Z. Yao, Analysis and control of edge effects in laser bending, Opt. Lasers Eng. 48 (2010) 305–315.
[34] J. Cheng, Y.L. Yao, Cooling effects in multiscan laser forming, J. Manuf. Processes 3 (2001) 60–72.
[35] S.P. Edwardson, E. Abed, K. Bartkowiak, G. Dearden, K.G. Watkins, Geometrical influences on multi-pass laser forming, J. Phys. D, Appl. Phys. 39 (2006) 382–389.
[36] H. Shen, Y. Shi, Z. Yao, Numerical simulation of laser forming of plates using two simultaneous scans, Comput. Mater. Sci. 37 (2006) 239–245.
[37] S.P. Edwardson, E. Abed, C. Carey, K.R. Edwards, G. Dearden, K.G. Watkins, Factors influencing the bend per pass in multi-pass laser forming, in: Laser Assisted Net Shape Engineering, Proc. LANE 5 (2007) 557–568.
[38] H. Shen, J. Zhou, Z.Q. Yao, Study on overlapping of two sequential scans in laser forming, Proc. Inst. Mech. Eng., Part C, J. Mech. Eng. Sci. 9 (2007) 993–997.
[39] T. Hennige, Development of irradiation strategies for 3D-laser forming, J. Mater. Process. Technol. 103 (2000) 102–108.
[40] D. Chen, S. Wu, M. Li, Deformation behaviours of laser curve bending of sheet metals, J. Mater. Process. Technol. 148 (2004) 30–34.
[41] C. Liu, Y. Yao, Optimal process planning for laser forming of doubly curved shapes, J. Manuf. Sci. Eng. 126 (2004) 1–9.
[42] Z. Peng, Y. Jingbo, Z. Xiongfei, Deformation behaviors of laser forming of ring sheet metals, Tsinghua Sci. Technol. 14 (2009) 132–136.
[43] K. Venkadeshwaran, S. Das, D. Misra, Finite element simulation of 3-D laser forming by discrete section circle line heating, Int. J. Eng. Sci. Technol. 2 (2010) 163–175.
[44] Q. Nadeem, S.J. Na, Deformation behavior of laser bending of circular sheet metal, Chin. Opt. Lett. 9 (2011) 051402.
[45] S. Chakraborty, V. Racherla, A. Nath, Parametric study on bending and thickening in laser forming of a bowl shaped surface, Opt. Lasers Eng. 50 (2012) 1548–1558.
[46] Q. Nadeem, W.J. Seong, S.J. Na, Process designing for laser forming of circular sheet metal, Chin. Opt. Lett. 10 (2012) 021405.
[47] Q. Nadeem, S.J. Na, An approach to form the dome shape by 3D laser forming, Chin. Opt. Lett. 11 (2013) 021402.
[48] F. Cook, D. Celentano, J. Ramos-Grez, Experimental-numerical methodology for the manufacturing of cranial prosthesis via laser forming, Int. J. Adv. Manuf. Technol. 86 (2016) 2187–2196.
[49] W. Li, Y.L. Yao, Numerical and experimental study of strain rate effects in laser forming, J. Manuf. Sci. Eng. 122 (2000) 445–451.
[50] F. Cook, V. Jacobsen, D. Celentano, J. Ramos, Characterization of the absorptance of laser irradiated steel sheets, J. Laser Appl. 27 (2015) 032006.
[51] L. Anand, Constitutive equations for the rate-dependent deformation of metals at elevated temperatures, J. Eng. Mater. Technol. 104 (1982) 12–17.
[52] P. Kozlowski, B. Thomas, J. Azzi, H. Wang, Simple constitutive equations for steel at high temperature, Metall. Trans. A, Phys. Metall. Mater. Sci. 23 (1992) 903–918.
[53] A.E. Huespe, A. Cardona, N. Nigro, V. Fachinotti, Visco-plastic constitutive models of steel at high temperature, J. Mater. Process. Technol. 102 (2000) 143–152.
[54] D. Celentano, D. Rosales, J. Peña, Simulation and experimental validation of tube sinking drawing processes, Mater. Manuf. Processes 26 (2011) 770–780.
[55] D. Celentano, Thermomechanical analysis of the tensile test: simulation and experimental validation, Struct. Eng. Mech. 13 (2002) 591–614.
[56] D. Celentano, Thermomechanical analysis of the Taylor impact test, J. Appl. Phys. 91 (2002) 3675–3686.
[57] D. Celentano, Thermomechanical simulation and experimental validation of wire drawing processes, Mater. Manuf. Processes 25 (2010) 546–556.